AIAA JOURNAL
Vol. 45, No. 6, June 2007

Flow Inside a Solid Rocket Motor with Relation to Nozzle Inlet Ablation

Toru Shimada*
Japan Aerospace Exploration Agency, Kanagawa 229-8510, Japan
Masumi Sekiguchi†
IHI Aerospace Engineering Company, Ltd., Gunma 370-2307, Japan
and
Nobuhiro Sekino‡
IHI Aerospace Company, Ltd., Gunma 370-2398, Japan

DOI: 10.2514/1.22952

Three-dimensional, single-phase (equilibrium two-phase) flows inside a solid rocket motor at three burn-back grain configurations are studied by computational fluid dynamics analyses of the Reynolds-averaged Navier–Stokes equations. The major concern is the relationship between the flowfield and the circumferentially periodic erosion pattern arising in the inlet region of the nozzle, which will be of help for better understanding of the surface recession mechanism. Obtained results for the first two cases show that, because the mass flux of the slot phase is notably large compared with that of the fin phase, a remarkable interphase gap in the amount of convection heating appears either in the throat or the exit cone. The peak heating rate appears, commonly to all cases, azimuthally in the slot phase and axially at the expansion ratio of about 0.9 upstream of the throat. The flow which comes out of a slot into a fin base region spreads toward the fin central part under the influence of the pressure gradient in the circumferential direction and forms a vortical flow tube of opposite rotation mutually with the flow which swirls out of the next slot. At the fin phase, because the proportionality relation is accepted between the total mass recession per unit area and the total convective heat mass transfer per unit area, there is little mechanical erosion, and corrosion is considered to be dominant. On the other hand, in the slot phase, surface recession which cannot be explained only by corrosion in a nozzle inlet nose exists. This surface recession has a very high possibility of having occurred by abrasion by the aluminum/alumina particles contained in the flow which comes out of the axial slot of grain and collides with the thermal protection system surface. It is expected that the periodic erosion pattern which synchronized with axial slots observed after the static-firing test is the result of such a mechanism ruling. In both the throat and the exit cone, it is thought irrespective of a phase that the effect of mechanical erosion is very small and corrosion or a so-called "chemical attack" is the dominant mechanism of surface recession.

Nomenclature

C_p	=	specific heat at constant pressure of gas
c	=	specific heat of condensed phase
$\vec{D}$	=	divergence of the velocity
e	=	total energy per unit volume
H	=	total enthalpy
k	=	turbulence energy
$\dot{m}$	=	mass efflux from the burning surface
Pr	=	Prandtl number
p	=	pressure
p_c	=	chamber pressure
Q	=	total heat load
$\boldsymbol{q}$	=	thermal conduction heat flux vector
$\dot{q}$	=	heat flux to the solid wall
R	=	gas constant
$\bar{R}$	=	gas constant for gas-particle equilibrium state
$\dot{r}$	=	linear burning rate
S^E	=	energy interaction between gas and condensed -phase
$\boldsymbol{S}^M$	=	momentum interaction between gas and condensed phase
T	=	temperature
t	=	time
$\boldsymbol{V}$	=	velocity vector
$\bar{\gamma}$	=	effective specific heats ratio
γ_g	=	specific heats ratio for gas phase
ε_c	=	recession amount due to corrosion
ε_m	=	recession amount due to mechanical erosion
ε_T	=	total amount of recession
μ	=	coefficient of viscosity
ρ	=	density
ρ_{prop}	=	propellant density
ρ_s	=	material bulk density
τ	=	burning period
$\bar{\bar{\tau}}$	=	shear stress tensor
ψ	=	loading ratio
ω	=	turbulent vorticity

Subscripts

g	=	gas phase
p	=	particle phase
t	=	turbulent

Presented as Paper 3891 at the 36th AIAA Fluid Dynamics Conference and Exhibit, Hyatt Regency San Francisco at Embarcadero Center, San Francisco, California, 5–8 June 2006; received 3 February 2006; revision received 23 October 2006; accepted for publication 28 November 2006.

*Professor, Institute of Space and Astronautical Science, 3-1-1 Yoshinodai, Sagamihara. Senior Member AIAA.
†Engineer, Engineering Department, 900 Fujiki, Tomioka.
‡Manager, Technologies Development Department, 900 Fujiki, Tomioka.

I. Introduction

A SOLID-PROPELLANT rocket motor (SRM) that is about 14 m long and about 2.5 m in the outer diameter and filled with about 70 tons of solid propellant in the high tensile strength steel case

has been offered for a static-firing test. A post-test evaluation of the static-test motor has revealed characteristic erosion synchronized with the axial slots of the propellant grain on the nozzle inlet region. As a result of that it is surmised that the internal three-dimensional flowfield due to the grain configuration affects the surface recession distribution of the thermal protection system (TPS) materials.

To protect the nozzle structural components from sever heating of high-speed combustion gas flow, TPS materials, thermoresistive material, such as graphite and 3-D carbon/carbon composite (3D-C/C), and thermoinsulative material, such as carbon phenolic fiber-reinforce plastic (CP-FRP or CFRP for short), are used as the throat insert and the nozzle liner materials. Generally such carbonaceous materials are ablated when exposed to SRM combustion gas and material mass is removed by surface corrosion and erosion. (In the case of CFRP, thermal decomposition occurs first and then the surface char layer is formed.) The cause of the surface recession can be divided into two major factors. One of them is so-called corrosion, in which the recession occurs due to the chemical reaction on the surface between combustion gas and the carbonaceous material. The other is mechanical recession called erosion. In this process shear force formed by a combustion gas or an impingement of condensed phase removes a part of TPS material mechanically. Therefore to estimate the ablating surface recession rate of TPS materials, it is required to know diffusion velocities of mass and heat across the boundary layer, as well as impinging particle influx produced by the SRM internal flow.

Although there is a strong need to know the SRM internal flow, major difficulties to fulfill it are attributed to the complexity of the flow outlined here.

In the combustion chamber, the working fluid consists of combusting gas, burning condensed-phase particles of metal fuel agglomerates (aluminum, Al), and their combustion products (aluminum oxides, Al_2O_3). Namely, the flow is a gas-particle, multiphase flow. The gas temperature is usually about 3500 K for a highly metallized solid propellant and the combustion pressure ranges from 50 to 150 atm.

Geometric configuration of propellant grain often has complex three dimensionality with axial or radial slots/fins in it. Because of the geometry, the secondary flow in the circumferential and the radial directions often develops. The shape of a burning surface changes during the course of burning usually at the rate of several millimeters per second. Vorticity is generated together with the injection of combustion gas from the burning surface and the flow is essentially rotational. The flow is at a low subsonic speed upstream in the combustion chamber and then accelerated gradually along the port. The flow is accelerated rapidly near the nozzle inlet, exceeding the speed of sound at the throat, and finally reaches supersonic speed in the exit cone. Furthermore, during the course of traveling, the gas element experiences the exchange of mass, momentum, and energy with condensed-phase particles. In addition, submerged nozzles are often used in the aft-dome area of SRM. It is known that reverse flow and circumferential flow exist in the submerged region due to grain slots and aft-dome configuration, as well as nozzle vectoring. Such nonaxisymmetric flow leads to asymmetric erosion of insulation material, sometimes affecting the propulsion performance, and furthermore, may lead to fatal troubles of the system.

Theoretical, experimental, and numerical approaches have been taken in the field of thermochemico aerodynamics of the SRM internal flow research. Although the use of a theoretical approach is usually limited to one- or two-dimensional simple flow, a closed-form solution is very helpful for the understanding of the propensity of the phenomena. For example, the solution of Culick [1] for the axisymmetric flow in SRM directly shows that the flow inside SRM is essentially rotational with vorticity shed from the burning surface.

In the literature, a number of reports on the flow phenomena inside SRM, especially on three-dimensional flow produced mainly by a configuration of the inner chamber geometry, can be found and several of them are summarized here.

Chaouat [2] researched the three-dimensional nature of the SRM internal flow (existence of circumferential flow) due to aft fins of the propellant grain. The research indicated that vortices shed from fins created nonaxisymmetric cross-sectional flow. This fact has been verified experimentally by Waesche et al. [3] and is a common characteristic of the internal flows of motors with fins. Three dimensionality of the flow or vortical flow is caused by mixing of the flows from fins with the core flow in the port and is intensified at the converging part of the submerged nozzle. Because the vortical flow affects the diffusion velocity of the mass and the heat crossing the surface boundary layer on the TPS materials, it causes circumferentially asymmetric ablation over the converging part of the nozzle. This effect is rapidly attenuated over the diverging part of the nozzle, throat downstream.

Johnston [4] conducted three-dimensional computational fluid dynamics (CFD) analyses of inviscid flows in a Titan solid rocket motor upgrade (SRMU). He studied both whether there is any development of circumferential flow inside radial slots at the segment-joint region of a SRMU and whether there is jetting from the axial slot of the forward propellant segment impinging onto the front face of the aft propellant segment.

Morstadt [5] conducted numerical simulations of the internal three-dimensional flows of the space shuttle reusable solid rocket motor (RSRM) using four turbulence models and two grids, and showed that the pressure drop propensity can significantly be affected by the turbulence model. He also showed that a pair of counter-rotating vortices in the axial direction shed from each of the forward fins of RSRM is the strongest source of the vortices in the axial direction in the core flow.

Waesche et al. [3], using 1/8 scale models in a water tunnel and in a cold-flow air wind tunnel, visualized the three-dimensional flow and quantified the velocity and its perturbation in the region of the motor-aft end of the advanced solid rocket motor (ASRM) of the space shuttle. They also investigated, using the same equipments, the effect of the propellant grain slots and aft-dome configuration on the flowfield.

Recently the efforts of researches are conducted on the vortex-shedding phenomena [6,7] and its effect on the acoustic instability in SRM [8].

In this article, three-dimensional, single-phase (equilibrium two-phase) flows inside a solid rocket motor at three burn-back grain configurations (0, 11, 27 s from the ignition) are studied by CFD analyses of the Reynolds-averaged Navier–Stokes equations (RANS). The major concern is the relationship between the flowfield and the circumferentially periodic erosion pattern arising in the inlet region of the nozzle, which will be of help for better understanding of the surface recession mechanism. It is also a purpose of the present paper to describe a mechanism of vortical flow generation in SRM.

II. Object of Analysis

The target SRM is about 14 m long and about 2.5 m in the outer diameter and consists of two segments, each of those filled with about 35 tons of solid propellant in the high tensile strength steel case. The maximum burning pressure is about 5 MPa and the effective burning period is about 50 s. A general view of the SRM is shown in Fig. 1. The configuration of the propellant grain in each segment is a fin-on-cylinder ("finocyl") type and has seven slots in the axial directions. The propellant is composed of AP/HTPB/Al ingredients with the weight percentages of 68/12/20, respectively, with a small amount of Fe_2O_3.

The nozzle of the SRM is submerged in and connected to the aft dome of the aft segment with the flexible joint so that it can be tilted for the thrust vectoring in the pitch and the yaw directions. As shown in Fig. 2, the TPS materials such as CFRP and 3D-C/C are furnished along the inner wall of the nozzle. A CFRP heat shield is placed upstream of the nozzle inlet, and the 3D-C/C throat insert is furnished downstream. The nozzle exit cone, with the expansion ratio of about 10 and the half-angle of 15 deg, consists of the forward cone with a CFRP liner and the aft cone of silica phenolic (SFRP).

As described before, post-test evaluation of the static-test motor revealed characteristic erosion synchronized with the axial slots of the propellant grain on the nozzle inlet region. A post-test

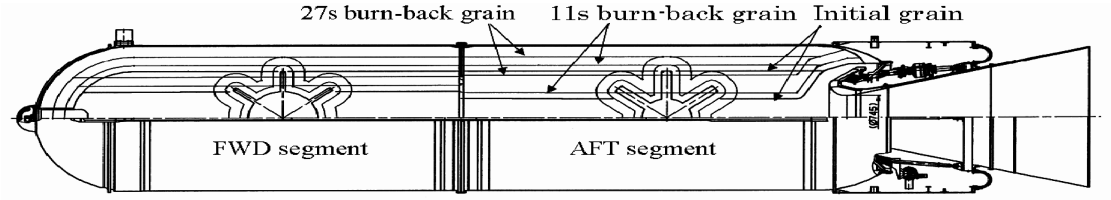

Fig. 1 General view of the target solid rocket motor, with three grain shapes (0, 11, and 27 s) indicated.

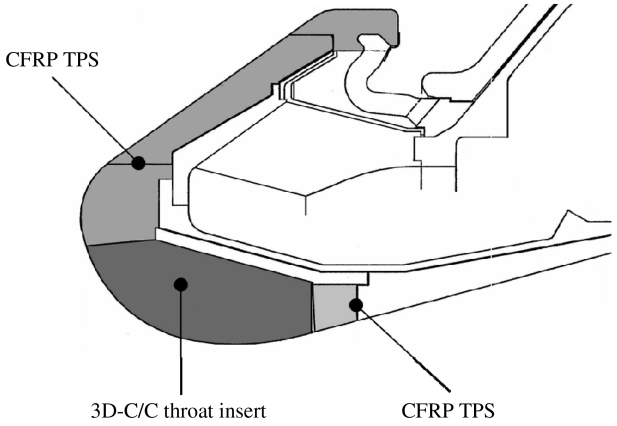

Fig. 2 General view of the nozzle inlet portion.

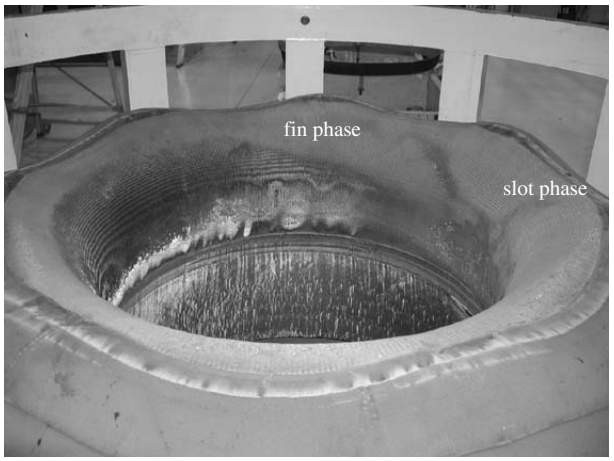

Fig. 3 Inlet portion of the nozzle after the static-firing test.

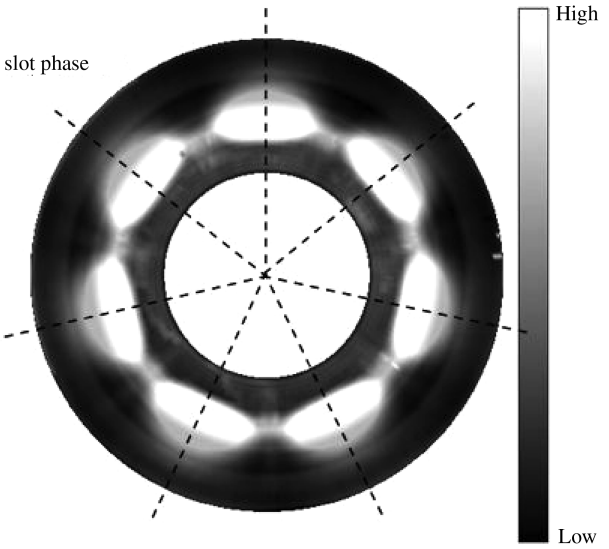

Fig. 4 Measured recession of the inlet portion.

photograph of the nozzle inlet is shown in Fig. 3 and measured surface recession of the TPS materials are depicted in Fig. 4. The total recession measurement has been conducted by using a laser distant-measurement device. Looking at the surface recession pattern, it is surmised that the internal three-dimensional flowfield due to the grain configuration affects the surface recession distribution of the TPS materials. In this research CFD analyses of the internal flow fields of the SRM have been performed to obtain a more accurate understanding of the relationship between the flowfield and the TPS surface recession.

It is well known that one of the major causes of the surface recession of TPS materials is a chemical attack of gaseous H_2O and CO_2 molecules to the solid carbon or char where surface-aligned flow is formed, although mechanical and/or particle impingement erosion can be significant depending on the location:

$$H_2O + C(s) \rightarrow H_2 + CO \qquad CO_2 + C(s) \rightarrow 2CO \qquad (1)$$

The factor which governs the rate of these reactions is roughly divided into two. One is chemical reaction rate mainly governed by the wall temperature, and another is a diffusion velocity by which steam and carbon dioxide contained in the core flow cross a boundary layer and are carried to the TPS surface. According to the past research [9–11], if the wall temperature exceeds 2000 K, the rates of these chemical reactions will become sufficiently quick, and it turns out that the diffusion speed of reactants is the rate-determining step. It is thought that the wall temperature of the nozzle inlet and throat is considered sufficiently high if it passes several seconds after the ignition. Therefore, the turbulent mass transfer coefficient across the boundary layer to the ablating surface can affect much of the recession rate of these materials. In the turbulent boundary layer of surface-aligned flow without separation, because it is thought that the so-called Reynolds analogy is materialized between heat transfer and substance transfer, the grade of diffusion of reactants is considered to be measured according to the grade of convective heat transfer here. From this viewpoint, in this paper we focus on the evaluation of the convective heat flux for the understating of the corrosion of TPS materials. Although the convective heat flux rate will be discussed later, please note that the purpose of the discussion is not the energy diffusion but the diffusion of reactants. Therefore the heating due to radiation and/or the deposition of the condensed phase are inapplicable. And because of the same reason, uniform and constant wall temperature suitable for a diffusion-controlled process is assumed in our computations.

It is considered that the total recession is the sum of the recession due to corrosion and that due to mechanical erosion. Therefore if one can evaluate one of two factors, the other can be estimated easily because the total recession has already been known experimentally. In this study, a correlation between the heat flux and the amount of recession is derived and used for discussion. The details of the correlation will be discussed later.

Considering that the grain configuration changes with the progression of combustion, flowfields with three different grain shapes, at the initial, 11 s burn-back and 27 s burn-back, corresponding to 0 mm burn-back, 100 mm burn-back, and 250 mm burn-back shapes, respectively, are computed (Fig. 1). Although in reality the TPS surface recedes back, it is assumed that no recession of the TPS surface is reflected in the computed geometries. It is not

considered that the major flow pattern formed in space bounded by a propellant grain and the surface of the nozzle inner wall changes dramatically according to the slight change of the nozzle inlet shape. Therefore constant inlet shape seems to be sufficiently reasonable for the understanding of the mechanism of surface recession. Furthermore, a precise inlet shape during the combustion cannot be determined because the mechanism of the surface recession is not clear at the moment. Taking into account these situations, as a first step, a constant inlet shape is assumed.

III. Method of Analysis

A. Assumptions

Though recent progress in computer technology has enabled one to perform numerical analyses dealing with complex physicochemical processes, the computational cost of three-dimensional simulation with various physical processes is still high. So the execution of the simulation needs cost performance assessment beforehand. Considering the purpose of the current research, we have adopted the assumptions and CFD modeling described here that are necessary for the objective achievement.

It is assumed that condensed-phase particle sizes are so small that particle velocity and temperature can follow those of the gas phase without delay, namely, equilibrium two-phase flow is considered. The chemical composition of the gas mixture including liquid Al_2O_3 is evaluated at the chamber condition by a chemical equilibrium code and assumed frozen in the flowfield. It means that no further change occurs in chemical composition of gases and particles both in the combustion chamber and on the nozzle surface. These two assumptions make it possible to formulate the problem by a flow of fictitious single-species gas with effective specific heats and mean-molecular weight (for details, see the next section). It is assumed that the transport coefficients of the gas mixture can be expressed by the power function of the temperature. The gas is assumed to follow the ideal gas equation of state. The flow is assumed turbulent and to be formulated by the RANS model, where the Reynolds stress tensor and the turbulent heat flux are evaluated with an eddy viscosity concept.

As described in the previous section, in this research, all cases set up wall temperature with 2500 K and assumed diffusion-controlled process.

The computational region is bounded by propellant grain and the surface of TPS materials of the nozzle inner wall, the center axis of the motor and the nozzle, the exit plane of the nozzle exit cone, and the boundary planes of the periodical conditions in the circumferential direction. Because the target motor has seven axial slots in the propellant grain, the one-seventh of the circumference is dealt as the computational region. Although, by using the further symmetry in the circumferential direction, it is possible to limit the region to one-fourteenth of the circumference, the authors have preferred to obtain the symmetry as the result of numerical computation by only imposing the periodical boundary conditions. It is to obtain solutions with as less limitation as possible.

B. CFD Analysis

The governing equations for the conservation of mass, momentum, and energy for combustion gas under the assumption of chemically frozen and constant specific heats can be written as follows:

$$\begin{aligned}
&\frac{\partial \rho_g}{\partial t} + \nabla \cdot [\rho_g \boldsymbol{V}_g] = 0 \\
&\frac{\partial \rho_g \boldsymbol{V}_g}{\partial t} + \nabla \cdot [\rho_g \boldsymbol{V}_g \otimes \boldsymbol{V}_g + p\vec{\vec{I}} - \vec{\vec{\tau}} - \vec{\vec{\tau}}_t] = \boldsymbol{S}^M \\
&\frac{\partial e_g}{\partial t} + \nabla \cdot [e_g \boldsymbol{V}_g + (p\vec{\vec{I}} - \vec{\vec{\tau}} - \vec{\vec{\tau}}_t) \cdot \boldsymbol{V}_g - \boldsymbol{q} - \boldsymbol{q}_t] = S^E
\end{aligned} \tag{2}$$

The total energy per unit volume of the gas phase e_g can be written using the equation of state for ideal gas as

$$e_g = \frac{p}{\gamma_g - 1} + \frac{1}{2}\rho_g |\boldsymbol{V}_g|^2 \tag{3}$$

In the same manner, the governing equations of the condensed phase are as follows:

$$\begin{aligned}
&\frac{\partial \rho_p}{\partial t} + \nabla \cdot [\rho_p \boldsymbol{V}_p] = 0 \qquad \frac{\partial \rho_p \boldsymbol{V}_p}{\partial t} + \nabla \cdot [\rho_p \boldsymbol{V}_p \otimes \boldsymbol{V}_p] = -\boldsymbol{S}^M \\
&\frac{\partial e_p}{\partial t} + \nabla \cdot [e_p \boldsymbol{V}_p] = -S^E
\end{aligned} \tag{4}$$

The relationship between the energy and temperature is as follows:

$$e_p = \rho_p c T_p + \tfrac{1}{2}\rho_p |\boldsymbol{V}_p|^2 \tag{5}$$

Because it is assumed that the velocity and the temperature of the particle phase follow those of the gas phase without delay in the present study, the velocity and the temperature can be replaced as follows:

$$\boldsymbol{V}_p = \boldsymbol{V}_g = \boldsymbol{V} \tag{6}$$

$$T_p = T_g = T \tag{7}$$

After the summation of Eqs. (2) and (4), then using the above equations, the governing equation for equilibrium two-phase flow can be obtained as

$$\begin{aligned}
&\frac{\partial \rho}{\partial t} + \nabla \cdot [\rho \boldsymbol{V}] = 0 \\
&\frac{\partial \rho \boldsymbol{V}}{\partial t} + \nabla \cdot [\rho \boldsymbol{V} \otimes \boldsymbol{V} + p\vec{\vec{I}} - \vec{\vec{\tau}} - \vec{\vec{\tau}}_t] = 0 \\
&\frac{\partial e}{\partial t} + \nabla \cdot [e\boldsymbol{V} + (p\vec{\vec{I}} - \vec{\vec{\tau}} - \vec{\vec{\tau}}_t) \cdot \boldsymbol{V} - \boldsymbol{q} - \boldsymbol{q}_t] = 0
\end{aligned} \tag{8}$$

where the density and the total energy can be written as

$$\rho = \rho_g + \rho_p \tag{9}$$

$$e = e_g + e_p \tag{10}$$

The equation of state is rewritten as

$$e = e_p + e_g = \left(\frac{\psi c}{R} + \frac{1}{\gamma_g - 1}\right) p + \frac{\rho}{2}|\boldsymbol{V}|^2 \tag{11}$$

$$p = \rho_g R T = \rho \frac{R}{1 + \psi} T \tag{12}$$

where ψ represents the loading ratio, that is, the ratio of the particle bulk density to the gas density,

$$\psi = \frac{\rho_p}{\rho_g} \tag{13}$$

which is determined by the mixture ratio of components in the composite solid propellant.

When the effective specific heats ratio and gas constant are determined as follows, finally we can get the formula of the same form as a single-species gas,

$$\frac{1}{\bar{\gamma} - 1} = \frac{1}{\gamma_g - 1} + \frac{\psi c}{R} \tag{14}$$

$$\bar{R} = \frac{R}{1+\psi} \tag{15}$$

Note that although the final expression is the same as that of a single-species ideal gas, the effect of the particle phase is included in the equations under the assumption of equilibrium two-phase flow.

To complete the equations for turbulent flow formulated by RANS equations with a k–ω turbulence model, two more equations for the turbulent model must be added to the above system of equations:

$$\frac{\partial \rho k}{\partial t} + \nabla \cdot (\rho \boldsymbol{V} k) = \nabla \cdot [(\mu + \sigma^* \mu_t) \nabla k] + \overleftrightarrow{\tau}_t : \nabla \boldsymbol{V} - \beta^* \rho k \omega$$
$$\frac{\partial \rho \omega}{\partial t} + \nabla \cdot (\rho \boldsymbol{V} \omega) = \nabla \cdot [(\mu + \sigma \mu_t) \nabla \omega] + \alpha \frac{\omega}{k} \overleftrightarrow{\tau}_t : \nabla \boldsymbol{V} - \beta \rho \omega^2 \tag{16}$$

The turbulent viscosity is evaluated by the relation:

$$\mu_t = \frac{\alpha^* \rho k}{\omega} \tag{17}$$

In the present computation, standard values are used for the parameters such as α^*, β^*, etc.

With an eddy viscosity concept, also called Boussinesq hypothesis, the Reynolds stress tensor $\overleftrightarrow{\tau}_t$ and the turbulent heat flux $\boldsymbol{q}_t$ are expressed by relations:

$$\overleftrightarrow{\tau}_t = -\frac{2}{3}(\rho k + \mu_t \nabla \cdot \boldsymbol{V}) \overleftrightarrow{I} + 2\mu_t \overleftrightarrow{D} \qquad \boldsymbol{q}_t = -\frac{C_p \mu_t}{Pr_t} \nabla T \tag{18}$$

Recent research on the turbulence model for solid rocket motor deals with the unsteady flowfield [12], but since we are interested in the steady flow only, the k–ω closure model is enough for the present purpose.

This system of partial differential equations is discretized by the finite-volume method to obtain a system of ordinary differential equations (ODE) expressing temporal change of the conservation variables in finite-volume cells. The system of the ODEs is further discretized in time into the delta form by an implicit method to obtain a steady-state flowfield as the time-asymptotic solution.

$$\overleftrightarrow{L}\,\overleftrightarrow{U}\,\Delta \boldsymbol{Q}_{i,j,k} = \overrightarrow{\mathrm{RHS}}_{i,j,k} \tag{19}$$

The right-hand side of this equation represents the physics, which is the explicitly evaluated amount of the temporal change of the conservation variables, and is determined by evaluating the net amount of fluxes at cell surfaces with known (nth step) quantities. The convection fluxes at cell interfaces are evaluated by the AUSM-DV-EF scheme [13] with the second-order accuracy attained by the MUSCL (monotonic upwind scheme for conservation laws) approach. On the other hand, diffusion fluxes are evaluated in a central-difference fashion. Having obtained the right-hand side terms, the implicitly evaluated amounts of the temporal change of the conservation variables $\Delta \boldsymbol{Q}_{i,j,k}$ are determined by reversing the symmetrically factorized two operators with the LU-SGS method [14]. The conservation variables at the $(n+1)$th step are then determined. By successively conducting the above procedure, temporal evolution of the flowfield is computed and with sufficient iterations a converged solution is obtained. The discussion in the present research is limited to such a "steady-state" flowfield.

The heat flux to the solid wall is evaluated from the temperature gradient in the surface-normal direction and a thermal conductivity under the condition of a given uniform wall temperature

$$\dot{q} = \frac{C_p \mu}{Pr} \frac{\partial T}{\partial n} \tag{20}$$

The coefficient of molecular viscosity is estimated by that of the chemical equilibrium gas-mixture composition at the chamber conditions and the temperature dependence of the viscosity coefficient is summarized by the form, $\mu = BT^A$.

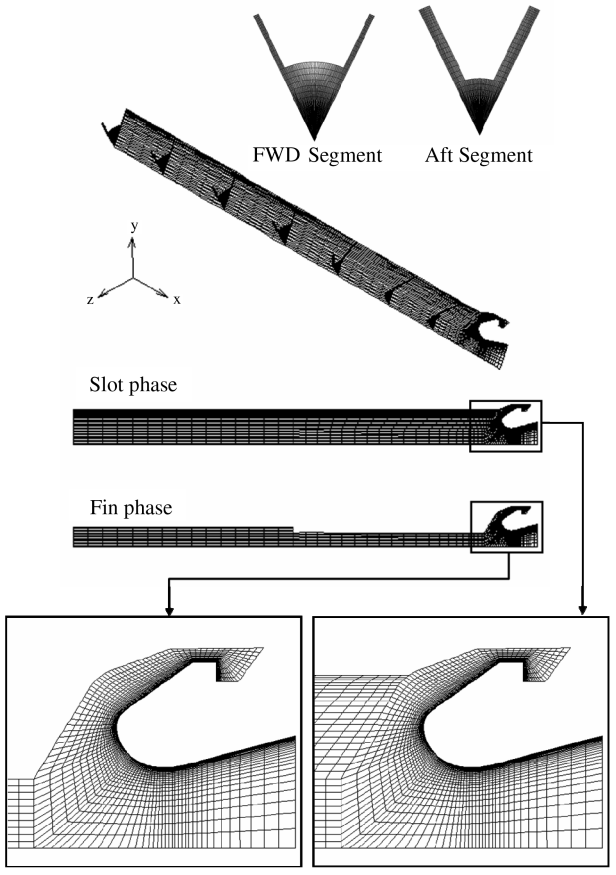

Fig. 5 Grid system for the initial grain configuration.

Propellant properties, combustion gas properties, the chamber conditions, and the wall temperature are used in the present computation commonly for three geometries of the initial, the 11 s burn-back, and the 27 s burn-back grains.

The grid systems for the initial grains are shown in Fig. 5 and similar grid systems are used for the other cases. The number of grid points are $100 \times 116 \times 105$ (about 1.22×10^6), $105 \times 116 \times 112$ (about 1.36×10^6), and $103 \times 116 \times 77$ (about 0.92×10^6), respectively. For all three, the minimum grid spacing on the nozzle surface is 0.1 μm, which is small enough for the viscous sublayer over the surface to be resolved.

There are two types of boundaries, namely, permeable and impermeable boundaries. While the former includes the propellant burning surfaces, the azimuthal boundaries, and the nozzle exit plane, the latter includes the TPS surfaces, the head-end and aft-end boundaries, and the axis of revolution.

On the burning surface, the combustion chamber pressure and the combustion temperature are fixed and the velocity direction is normal to the surface. The mass flux through the surface is determined by multiplying the propellant density by the linear burning rate evaluated with an experimental burning rate formula,

$$\dot{m} = \rho_{\mathrm{prop}} a p_c^n \tag{21}$$

The erosive burning effect in the real motor appears only in the early period of burning and is not considered in this study.

On the azimuthal boundaries, the periodic boundary conditions are imposed, and on the nozzle exit plane so are the supersonic outflow conditions. On the head-end and the aft-end boundaries, the slip condition of the velocity is imposed and so are vanishing normal gradients of both the temperature and the pressure. On the axis of revolution, all fluxes are zero.

In the numerical procedure these boundary conditions are realized by the use of ghost cells prepared on the other side of the boundary, giving physical quantities to the ghost cells according to the corresponding boundary conditions at each time step, and the use of

the ghost cell values at the calculation of numerical fluxes on the boundary. In some cases, for example, on the axis of revolution, boundary conditions can be imposed directly in the flux evaluation.

Total convection heating per unit area is estimated by a timewise integration of the convection heating distributions over the TPS surfaces at the three instances (0, 11, 27 s) obtained by the CFD analyses. Because the combustion pressure is almost constant between 0 to 25 s, the convection heating distribution at every moment is evaluated by a timewise linear interpolation during the period. In the later time, it is estimated by an interpolation weighted by the pressure ratio to the power of 0.8, which is a natural selection as a correlation of the turbulent forced convection heat transfer in a tube as also employed in Bartz's formula [15]. The pressure ratio is taken to that of the 27 s burn-back case.

IV. Results and Discussion

A. Convective Heat Flux

Computed results of the convective heat flux distributions over TPS surfaces are shown in Fig. 6 for the three grain shapes. On the surface in the submerged region (not shown in Fig. 6), the heat flux is relatively small and gradually increases downstream. The heat flux variation in the azimuthal direction is small in this region. Around the inlet nose, there is drastic change in the azimuthal direction. Whereas the convective heating is, especially for the initial and the 11 s burn-back shapes, relatively mild in the center of the fin phase, abrupt increases of the heat flux are observed in the slot phase up to the throat for all grain shapes. Especially for the 11 s burn-back case, corresponding to the slot growth, a higher heating rate of the slot phase expands in the throat portion. On the other hand, the domain showing the similar characteristic as a fin phase becomes narrower near the throat. The description above applies also to the 27 s burn-back shape, but there is a smaller difference of the fin phase and the slot phase compared with other cases. The peak heating rate appears, commonly to all cases, azimuthally in the slot phase and axially at the expansion ratio of about 0.9 upstream of the throat. Heating rates decrease rapidly in the nozzle expansion portion downstream of the throat with an azimuthal differential retained.

B. Oil Flow Patterns

Oil flow patterns on the TPS surfaces are obtained by calculation and shown in Fig. 7. An oil flow here is what is calculated as a curve which has the direction of a surface friction stress in a tangent. In a submerged part, oil flow patterns of the two cases of the initial grain and the 27 s burn-back grain clearly differ from that of the 11 s burn-back grain case. Whereas, in the former, the surface flow is flowing

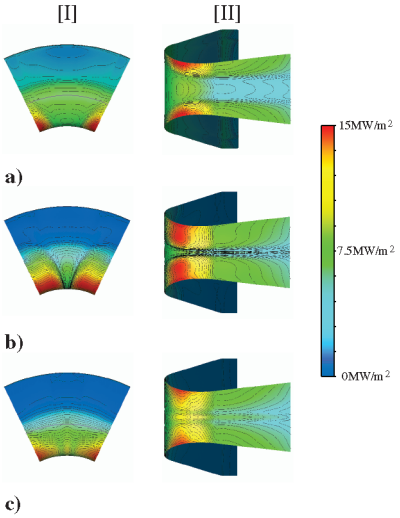

Fig. 6 Convective heat flux distributions over TPS surfaces. a) Initial grain case; b) 11 s burn-back grain case; c) 27 s burn-back grain case. I Inlet portion, TPS material boundary shown by pink line; II nozzle throat region.

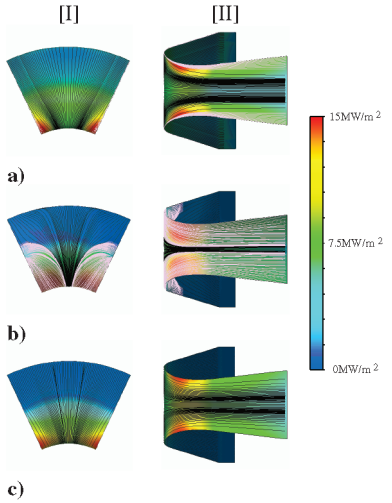

Fig. 7 Computed oil flow patterns on TPS surfaces, with convective heat flux distributions. a) Initial grain case; b) 11 s burn-back grain case; c) 27 s burn-back grain case. I Inlet portion; II nozzle throat region.

almost in line with a plane of constant azimuthal angle, in the latter, big separation domains are observed to exist in the nozzle inlet part and the flow from the upstream region is flowing so that the domain may be bypassed, which contracts toward the center of a fin phase. Both in the initial grain case and in the 11 s burn-back grain case, newly generated oil flow lines from the stagnation point domain on the TPS surface are shown by pink-colored lines. They suggest the existence of a colliding stream to a stagnation point domain. It has appeared clearly for the slot phase and the fin phase to differ on the starting domain of the oil flow both in the throat region and in the nozzle expansion part. In the 27 s burn-back case, a colliding stream is not observed; however, in this case one can also grasp the tendency of the flow convergence to the center of a fin.

C. Mechanism of Vortical Flow Tube Generation

A swirling flow which surrounds a nozzle inlet part is observed downstream of both of the side walls of a fin, and this situation is shown in Fig. 8. The flow which came out from the slot bottom forms the swirling flow, as it flows into the domain where the rear of the grain is scooped out by the aft-end cavity. When one sees toward the direction of a flow, the flow which comes out from the right-hand side wall of a fin appears to rotate counterclockwise and from the left-hand side wall of a fin conversely forms the flow which rotates clockwise. The initial grain case of a swirling flow is the clearest, and it seems to lose plainness with progress of time.

The domains of high vorticity, neighboring velocity vectors, and the amount of surface recession are indicated in Fig. 9, using the result of an initial grain case, to investigate the flowfield near the nozzle inlet. As drawn in Fig. 9, there is a flow which spreads in the direction of a fin where it came out of the slot, and on the other hand, there is a flow from a submerged region or a fin base surface, and it seems that the vorticity is made because of their velocity difference.

Domains of high vorticity (an equivorticity contour), streamlines shed from points on two azimuth angles near the slot exit, and a measured recession amount of nozzle TPS are displayed in Fig. 10 for the case of the 11 s burn-back grain. It can be observed in Fig. 10 that there is a colliding flow on the high recession portion of the TPS. Vorticity is generated where a flow appears from a slot in the cavity domain, as seen in Fig. 9. Moreover, in addition to this, it is generated at the place where a flow collides with the TPS surface. It seems that these vortical flows have merged in midair (not shown). It turns out that the vortical flow tube is further maintained also in the nozzle exit cone exceeding the nozzle throat.

In Fig. 11, the pressure distribution and the mass flux distribution in the inflow surface to the cavity region are shown about the initial grain case. This figure shows that mass flux of the slot phase is larger than that of the fin phase, and that a pressure gradient in the azimuthal

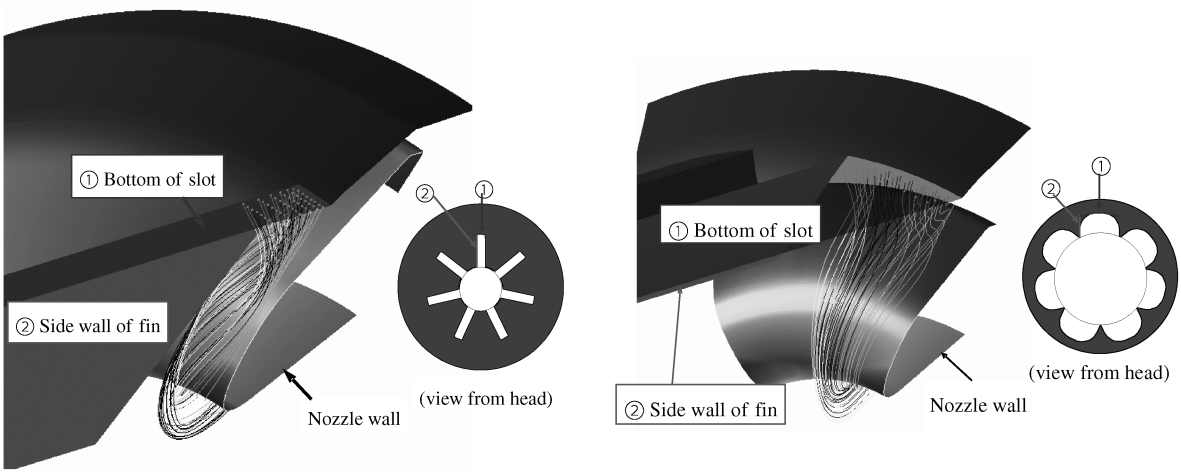

Fig. 8 Streamlines shed from the bottom plane of the slot for the cases of the initial grain shape (left) and the 27 s burn-back grain shape (right).

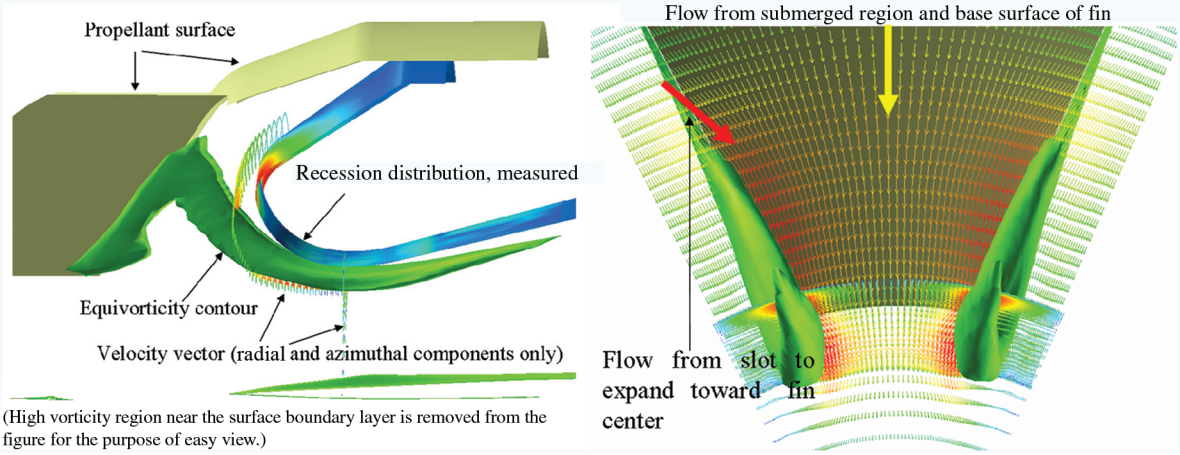

Fig. 9 Flowfield in the nozzle inlet region for the initial grain case. An equivorticity contour, velocity vectors, and recession erosion distribution are shown, (left) side view, (right) front view.

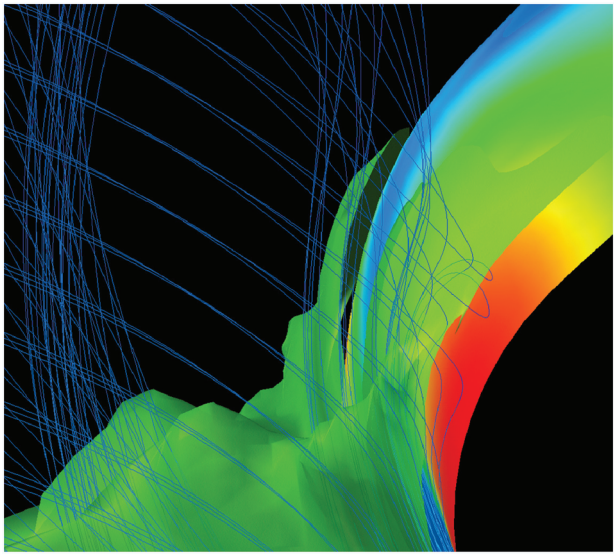

Fig. 10 Flowfield in the nozzle inlet region for the 11 s burn-back grain case. Shown is an equivorticity contour (green), with some streamlines and erosion distribution of the nozzle surface. Close-up view of flow impingement.

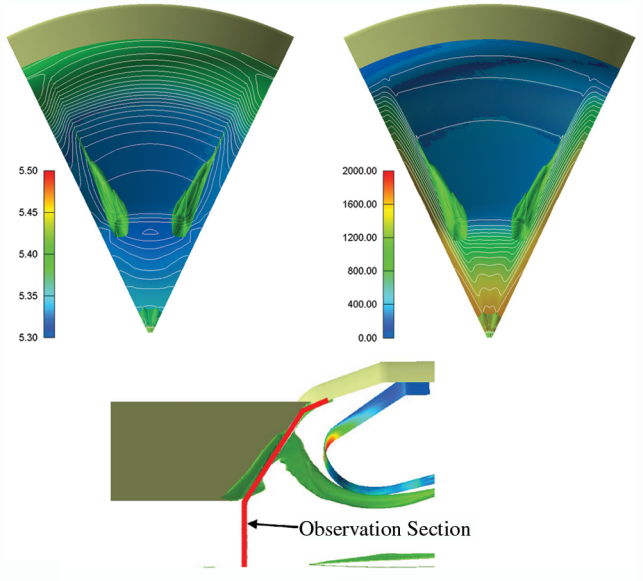

a) b)

Fig. 11 Pressure distributions and mass flux distributions in an observation section with an equivorticity contour shown. a) Pressure distribution (MPa); b) mass flux distribution (kg/m^2-s) of the initial grain shape.

direction exists at the exit of the slot. The flow which flows into the cavity region from the slot has large mass flux and high static pressure at the exit of the slot. In addition to this, because a low-pressure part exists in the base region of a fin, the pressure gradient appears, and according to that, the velocity component going toward the center of a fin arises. In the first place, in this domain, because subsonic contraction of the flow which goes to the nozzle throat is a dominant phenomenon, the velocity is naturally going in the direction of the central axis. Because another flow which spreads toward the center of a fin, by the same mechanism as the above, also arises from the next slot on both sides of the fin, the flows counter each other in the base region of the fin. Therefore, these two flows will circumferentially contract the flow of the fin phase coming from the submerged region, and recompression occurs in a somewhat lower position in the radial coordinate. It is thought that the flow is caused to return to the slot side conversely by this, and still more finally, it unites to the main port flow. This is how a vortical flow tube is formed in the nozzle.

It should be noted that the swirling flow mechanism described above is totally different from that reported in [2].

D. Mechanism of Recession Pattern

By evaluating the relationship between the flowfield and the surface recession of nozzle TPS, the periodic recession mechanism of the nozzle inlet of the static-firing test motor is considered.

As described in the former sections, it is assumed that the surface temperature is sufficiently high, so that the diffusion rate of reactants controls the surface recession rate of TPS material and in the turbulent boundary layer of the surface-aligned flow without separation, the grade of diffusion of reactants is considered to be measured according to the grade of convective heat transfer.

First, it is assumed that the total amount of the recession ε_T is expressed with the sum of the recession due to corrosion ε_c and the recession due to mechanical erosion ε_m, that is,

$$\varepsilon_T = \varepsilon_c + \varepsilon_m, \qquad (\varepsilon_c \geq 0, \varepsilon_m \geq 0) \tag{22}$$

Next, it is assumed that there should be little mechanical erosion in the fin phase considering the above observation of the flowfield and the measurement of the surface recession, and that the surface recession in the fin phase shall be governed by corrosion only.

Then, in the fin-phase plane, a correlation among these quantities may be obtained by assuming the recession due to corrosion ε_c be a function of the total heat load Q, the mainstream total enthalpy H (J/kg), and the bulk density of the TPS surface ρ_s (kg/m^3), namely,

$$\varepsilon_c = f(\rho_s, Q, H) \tag{23}$$

Performing a simple dimensional analysis of this formula shows that it is appropriate to investigate correlation between the amount of mass recession per unit area $\rho_s\varepsilon_c$ (kg/m^2) and the heat-mass transfer per unit area Q/H (kg/m^2). As a result, having set the densities of the CFRP char layer and 3D-C/C, respectively, to 1000 and 2000 kg/m^3, using the calculated value of the total heat load, and the measured value of the amount of surface recession, the following proportionality relation as shown in Fig. 12 among such quantities exists in the fin phase:

$$\rho_s\varepsilon_c = 0.20 \cdot \frac{Q}{H} \tag{24}$$

In the above expressions, a definition is given to the total amount of heating, or the total heat load per unit area, Q (J/m^2) as an integration value of the convective heat flux $\dot{q}$ (W/m^2) to cover the total burning time τ (s). The total recession ε_T (m) is defined as an integration value over the total burning time of the recession rate $\dot{r}$ (m/s) of the surface of TPS, namely,

$$Q = \int_0^\tau \dot{q}\, \mathrm{d}t \tag{25}$$

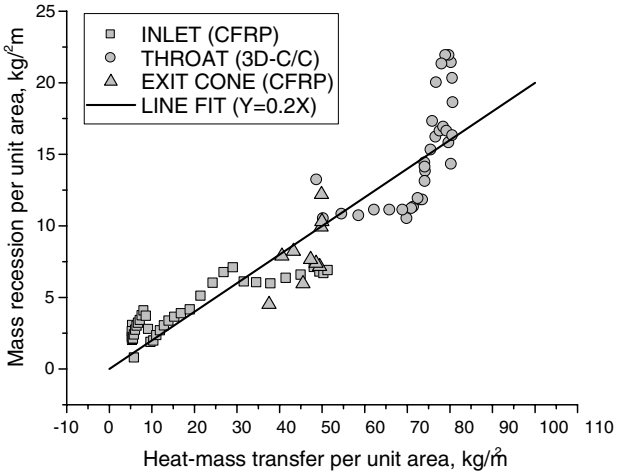

Fig. 12 Correlation of mass recession per unit area and heat-mass transfer per unit area in the fin phase.

$$\varepsilon_T = \int_0^\tau \dot{r}\, \mathrm{d}t \tag{26}$$

The correlation of the corrosion, Eq. (24), is obtained in the fin-phase plane assuming that the total recession in the phase is governed only by the corrosion. Next we apply the correlation all over the surface to get the estimated amount of corrosion ε_c. This can be done simply by using the computed local values of Q with the material bulk density ρ_s according to the position. The recession amount due to mechanical erosion can be calculated by subtracting ε_c from the measured total recession ε_T, that is,

$$\varepsilon_m = \varepsilon_T - \varepsilon_c \tag{27}$$

Note that in the place where ε_m becomes negative, $\varepsilon_m = 0$ is imposed.

The result obtained is shown in Fig. 13. Whereas the domain of very remarkable mechanical erosion exists in the nose of the inlet, it turns out that it hardly exists in the throat or the exit cone. The remarkable domain of this mechanical erosion is a domain where a flow collides with the TPS surface, as an oil flow pattern shows. In this domain, because the Mach number of colliding flow is low, convective heat transfer is small; therefore recession by corrosion is at most about 1/3 of that by mechanical erosion. Because , as with the heat flux, neither the surface shear force nor the dynamic pressure is thought to be high, mechanical erosion by gas flow is considered small there. Moreover, because the ply angle is large enough, as for CFRP of this domain, it is expected that permeability of the char layer is comparatively high. Furthermore, because the static pressure of external gas flow is high within the combustion chamber, it is thought that a pressure difference with pyrolysis gas inside the ablator is small. From these situations, a possibility that the char layer will start

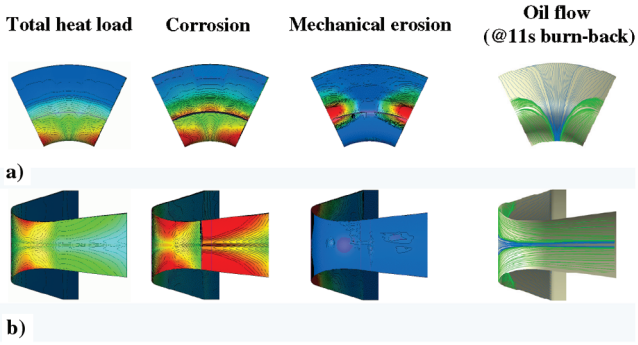

Fig. 13 Calculated total heat load, estimated amounts of corrosion and mechanical erosion, oil flow pattern. a) inlet portion and b) nozzle throat region.

spallation in this place is thought to be low. By synthesizing the above, it is reasonable to think that abrasion by aluminum/alumina particles contained in the flow which collides with this domain is the main cause of this mechanical erosion.

Because the flow in this region becomes surface aligned in the second half of the burning period, reasoning of smoothing the TPS surface after the static-firing test can be understood. However, on the other hand, it is checked from the investigation of aluminum/alumina slag in three static-firing tests of the SRM that only several kilograms remain to total propellant weight of 72 tons. This quantity is usually less than $1/10$ of the level of SRM of this scale. It is thought that the design of the particle size combination of AP in the composite propellant has realized such high combustion efficiency. Although, strictly speaking, it is necessary to investigate the particle size distribution of agglomerates experimentally, little of the slag amount and the smoothness of erosion have suggested that a small particle's existence rate is high in the target SRM.

V. Conclusions

The following knowledge has been obtained using the present result of the three-dimensional CFD analyses carried out to investigate the relation between the internal flowfield and the surface recession of the nozzle inlet TPS observed in the static-test motor.

For about 10–20 s after the ignition, because the mass flux of the slot phase is notably large compared with that of the fin phase, a remarkable interphase gap in the amount of convection heating appears either in the throat or the exit cone. The peak heating rate appears, commonly to all cases, azimuthally in the slot phase and axially at the expansion ratio of about 0.9 upstream of the throat. Heating rates decrease rapidly in the nozzle expansion portion downstream of the throat with an azimuthal differential retained. The flow which comes out of a slot into a fin base region spreads toward the fin central part under the influence of the pressure gradient in the circumferential direction and forms a vortical flow tube of opposite rotation mutually with the flow which swirls out of the next slot. These again promote the tendency for the rate of heating of the slot phase to become high. It should be noted that the swirling flow mechanism described above is totally different from that reported previously in the literature. At the fin phase, because the proportionality relation is accepted between the total mass recession per unit area and the total heat-mass transfer per unit area, there is little mechanical erosion, and corrosion is considered to be dominant. On the other hand, in the slot phase, a surface recession which cannot be explained only by corrosion in a nozzle inlet nose exists. This surface recession has a very high possibility of having occurred by abrasion by the aluminum/alumina particles contained in the flow which comes out of the axial slot of grain and collides with the TPS surface. It is expected that the periodic erosion pattern which synchronized with the axial slots observed after the static-firing test is the result of such a mechanism ruling over. In both the throat and the exit cone, it is thought irrespective of a phase that the effect of mechanical erosion is very small and corrosion or a so-called chemical attack is the dominant mechanism of surface recession.

Acknowledgments

This paper is partially based on the result of the collaborative project (FY2002 and FY2003) of former Institute of Space and Astronautical Science (ISAS), National Aerospace Laboratory of Japan (NAL), and National Space Development Agency of Japan (NASDA), which are now united as Japan Aerospace Exploration Agency (JAXA). The authors express gratitude to Mihoko Fukunaga of IHI Aerospace Company, Ltd., for her valuable support. This research is partially supported by JAXA Grant U4-UK-4K2-USRPJ-1002.

References

[1] Culick, F. E. C., "Rotational Axisymmetric Mean Flow and Damping of Acoustic Waves in a Solid Propellant Rocket," *AIAA Journal*, Vol. 4, No. 8, 1966, pp. 1462–1464.

[2] Chaouat, B., "Flow Analysis of a Solid Propellant Rocket Motor with Aft Fins," *Journal of Propulsion and Power*, Vol. 13, No. 2, March–April 1997, pp. 194–196.

[3] Waesche, R. H. W., Marchman, J. F., and Kuppa, S., "Effects of Grain and Aft-Dome Configuration on Aft-End SRB Internal Flows," *Journal of Propulsion and Power*, Vol. 7, No. 2, March–April 1991, pp. 163–170.

[4] Johnston, W. A., "A Computational Fluid Dynamics Analysis of the Internal Flow in a Titan SMRU," AIAA Paper 90-2079, July 1990.

[5] Morstadt, R. A., "A 3-D CFD Analysis of the Space Shuttle RSRM with Propellant Fins @ 1 s Burn-back," AIAA Paper 2003-5105, July 2003.

[6] Vulliot, F., "Vortex-Shedding Phenomena in Solid Rocket Motors," *Journal of Propulsion and Power*," Vol. 11, No. 4, 1995, pp. 626–639.

[7] Ballereau, S., Godfroy, F., Orlandi, O., and Ballion, D., "Numerical Simulations and Searching Methods of Thrust Oscillations for Solid Rocket Boosters," AIAA Paper 2006-4425, July 2006.

[8] Flandro, G. A., "Effects of Vorticity on Rocket Combustion Stability," *Journal of Propulsion and Power*, Vol. 11, No. 4, 1995, pp. 607–625.

[9] Delaney, L. J., Eagleton, L. C., and Jones, W. H., "A Semiquantitative Prediction of the Erosion of Graphite Nozzle Inserts," *AIAA Journal*, Vol. 2, No. 8, 1964, pp. 1428–1433.

[10] Keswani, S. T., and Kuo, K. K., "An Aerothermochemical Model of Carbon-Carbon Composite Nozzle Recession," *Structures, Structural Dynamics and Materials Conference*, Collection of Technical Papers, Pt. 1 (A83-29729 12-39), AIAA, New York, 1983, pp. 348–358; also AIAA Paper 1983-910.

[11] Borie, V., Brulard, J., and Lengellé, G., "Aerothermochemical Analysis of Carbon-Carbon Nozzle Regression in Solid-Propellant Rocket Motors," *Journal of Propulsion and Power*, Vol. 5, No. 6, 1989, pp. 665–673.

[12] Flandro, G. A., Cai, W., and Yang, V., "Turbulent Transport in Rocket Motor Unsteady Flowfield," *Solid Propellant Chemistry, Combustion, and Motor Interior Ballistics*, edited by V. Yang, T. Brill, and W. Ren, Vol. 185, Progress in Astronautics and Aeronautics, AIAA, Reston, VA, 2000, pp. 837–858.

[13] Shimada, T., and Sekino, N., "Numerical Simulations of Flows Around Re-Entry Vehicle and Evaluation of Heating Rate," SP-34, NAL, 1997, pp. 83–88 (in Japanese).

[14] Yoon, S., and Jameson, A., "Lower-Upper Symmetric-Gauss-Seidel Method for the Euler and Navier-Stokes Equations," *AIAA Journal*, Vol. 26, No. 9, 1988, pp. 1025–1026.

[15] Bartz, D. R., "A Simple Equation for Rapid Estimation of Rocket Nozzle Convective Heat Transfer Coefficient," *Jet Propulsion*, Vol. 27, No. 1, 1957, pp. 49–51.

S. Aggarwal
Associate Editor